

THE REST-FRAME ULTRAVIOLET STRUCTURE OF $0.5 < z < 1.5$ GALAXIES

NICHOLAS A. BOND¹, JONATHAN P. GARDNER¹, DUILIA F. DE MELLO², HARRY I. TEPLITZ³, MARC RAFELSKI³,
ANTON M. KOEKEMOER⁴, DAN COE⁴, NORMAN GROGIN⁴, ERIC GAWISER⁵, SWARA RAVINDRANATH⁶, AND CLAUDIA SCARLATA⁷

¹ Cosmology Laboratory (Code 665), NASA Goddard Space Flight Center, Greenbelt, MD 20771, USA

² Physics Department, The Catholic University of America, Washington, DC 20064 USA

³ IPAC, California Institute of Technology, Pasadena, CA 91125, USA

⁴ Space Telescope Science Institute, 3700 San Martin Drive, Baltimore, MD 21218, USA

⁵ Department of Physics and Astronomy, Rutgers University, Piscataway, NJ 08854, USA

⁶ Inter-University Centre for Astronomy and Astrophysics, Pune, India

⁷ Minnesota Institute for Astrophysics, School of Physics and Astronomy, University of Minnesota, Minneapolis, MN 55455, USA

Received 2013 November 25; accepted 2014 March 26; published 2014 July 22

ABSTRACT

We present the rest-frame UV wavelength dependence of the Petrosian-like half-light radius (r_{50}), and the concentration parameter for a sample of 198 star-forming galaxies at $0.5 < z < 1.5$. We find a $\sim 5\%$ decrease in r_{50} from 1500 Å to 3000 Å, with half-light radii at 3000 Å ranging from 0.6 kpc to 6 kpc. We also find a decrease in concentration of ~ 0.07 ($1.9 < C_{3000} < 3.9$). The lack of a strong relationship between r_{50} and wavelength is consistent with a model in which clumpy star formation is distributed over length scales comparable to the galaxy's rest-frame optical light. While the wavelength dependence of r_{50} is independent of size at all redshifts, concentration decreases more sharply in the far-UV (~ 1500 Å) for large galaxies at $z \sim 1$. This decrease in concentration is caused by a flattening of the inner $\sim 20\%$ of the light profile in disk-like galaxies, indicating that the central regions have different UV colors than the rest of the galaxy. We interpret this as a bulge component with older stellar populations and/or more dust. The size-dependent decrease in concentration is less dramatic at $z \sim 2$, suggesting that bulges are less dusty, younger, and/or less massive than the rest of the galaxy at higher redshifts.

Key words: cosmology: observations – galaxies: formation – galaxies: high-redshift – galaxies: structure

Online-only material: color figures

1. INTRODUCTION

Observations of galaxies at rest-frame ultraviolet wavelengths ($\lambda \sim 1500$ Å) are important for tracing the evolution of star formation and dust obscuration. Until recently, the study of the structural properties of galaxies in the rest-frame ultraviolet has focused on $z \gtrsim 2$, as wavelengths < 3000 Å and redward of the Lyman Break are easily accessible in the observed-frame optical using the Advanced Camera for Surveys (hereafter, ACS, Ford et al. 2003) on the *Hubble Space Telescope* (HST).⁸ Furthermore, the *Galaxy Evolution Explorer* (Martin et al. 2005) allows for the study of galaxy structure at $z \lesssim 0.5$ (e.g., Kuchinski et al. 2000; Heckman et al. 2005; Taylor-Mager et al. 2007). With the installation of the Wide Field Camera 3 (hereafter WFC3), including the UVIS channel, we now have the capability to directly observe the UV emission from hot stars in galaxies at $0.5 < z < 1.5$, a redshift interval that spans about one third of the history of the universe.

Recently published studies of the morphological properties of $0.5 < z < 1.5$ galaxies are drawn largely from the Cosmic Assembly Near-IR Deep Extragalactic Legacy Survey (CANDELS, Grogin et al. 2011; Koekemoer et al. 2011), which observed ~ 0.2 deg² of sky in the optical and near-infrared with HST/ACS and HST/WFC3, respectively. In one such study, Wuyts et al. (2012) performed resolved spectral energy distribution (SED) fitting of 323 star-forming galaxies and found that the majority of recent star formation at $0.5 < z < 1.5$ is occurring in clumps at or near the effective radius. These

observations are consistent with theoretical models of gas-rich turbulent disks where clumps are supported by infalling cold streams of gas (Bournaud et al. 2007; Bournaud & Elmegreen 2009). There are alternative models involving mergers (e.g., Robertson & Bullock 2008), which may be important for a subset of galaxies at these redshifts, but fragmented structures in sources with clear rotation curves suggest that this is not the dominant mechanism (Genzel et al. 2008; Fruchter & Sosey 2009; Law et al. 2009; Shapiro et al. 2009).

At higher redshifts, rest-frame UV imaging with ACS reveals that most $z > 2$ star-forming galaxies are clumpy, disturbed and disk-like in the rest-frame UV, with only $\sim 30\%$ having light profiles consistent with galactic spheroids (e.g., Ferguson et al. 2004; Elmegreen & Elmegreen 2005; Lotz et al. 2006; Ravindranath et al. 2006; Petty et al. 2009). These studies find typical half-light radii of ~ 2 kpc at $z \sim 2-3$ and a size evolution that scales approximately as $H^{-1}(z)$. Although the UV wavelength dependence of galaxy structure has not been studied at high redshift, such studies have been carried out on well-resolved galaxies in the local universe. Taylor-Mager et al. (2007) found that morphology changes occur as one observes bluer in the UV, with galaxies becoming less concentrated, clumpier and more asymmetric.

We can obtain a clearer picture of the young stars in galaxies at $0.5 \lesssim z \lesssim 1.5$ by studying their rest-frame UV emission at $\lambda \sim 1000-4000$ Å. Previous studies of star-forming galaxies in this redshift range were performed without the aid of observed-frame UV imaging (e.g., Bruce et al. 2012; Wuyts et al. 2012, 2013) or with relatively shallow imaging in a single filter (Voyer 2011; Rutkowski et al. 2012). In this paper, we use data taken as part of a program (GO 11563, PI: Teplitz) to obtain UV imaging of the Hubble Ultra Deep Field (hereafter UVUDF) and study intermediate-redshift galaxy structure in

⁸ Based on observations made with the NASA/ESA *Hubble Space Telescope*, obtained (from the Data Archive) at the Space Telescope Science Institute, which is operated by the Association of Universities for Research in Astronomy, Inc., under NASA contract NAS 5-26555. These observations are associated with program number HST-GO-12534.

the F336W, F275W, and F225W filters, complementing existing optical and near-IR measurements from the 2012 Hubble Ultra Deep Field (HUDF12; Ellis et al. 2013) survey. We use AB magnitudes throughout and assume a concordance cosmology with $H_0 = 71 \text{ km s}^{-1} \text{ Mpc}^{-1}$, $\Omega_m = 0.27$, and $\Omega_\Lambda = 0.73$ (Spergel et al. 2007). With these values, $1'' = 8.0$ physical kpc at $z = 1$.

2. DATA AND METHODOLOGY

The UVUDF data and the optical Hubble Ultradeep Field (UDF; Beckwith et al. 2006) are both contained within a single deep field in the Great Observatories Origins Deep Survey South. The new UVUDF data include imaging in three filters (F336W, F275W, and F225W), obtained in 10 visits, for a total of 30 orbits per filter. In addition, from the UDF, we make use of deep drizzled images taken in the observed optical with the F435W, F606W, and F775W filters. What follows is a brief summary of the observation strategy, data reduction, and catalog generation. For much greater detail on these procedures, see Teplitz et al. (2013, UVUDF), Beckwith et al. (2006, UDF), and (M. Rafelski et al., in preparation).

The first half of the UVUDF observations were taken with 2×2 onboard binning and without any artificial background added to the exposures. In the second half, in order to mitigate the effects of charge transfer inefficiency (CTI), the observations were done without binning and with an artificial “post-flash.” We use only the second half of the observations for the following analysis. Although the effects of the CTI are mitigated by the post-flash, it could potentially still alter the apparent sizes of galaxies. We discuss and test this possibility in Section 2.3.

We reduced and calibrated the individual exposures incorporating overall bias frames, custom CTI-corrected dark frames and hot pixel removal (to be described in M. Rafelski et al., in preparation), flat-fielding, and background subtraction that includes the removal of the post-flash. After applying a CTI correction to the raw data (using v1.0 of the standard CTI correction tool⁹), we combined the exposures using MultiDrizzle (Koekemoer et al. 2002), with a pixfrac of 0.8 and a square kernel, to produce final drizzled images with a pixel scale of 30 mas. Details of the image combination are the same as those described in Koekemoer et al. (2011). In order to ensure accurate alignment of the UV imaging with the UDF (Beckwith et al. 2006), the WFC3 exposures were individually aligned to the UDF *B*-band catalog.

We construct a source catalog (M. Rafelski et al., in preparation), following a procedure similar to the Ultradeep Field catalog (Coe et al. 2006). All objects are detected using SExtractor (Bertin & Arnouts 1996) on an image that is the weighted sum of the F435W, F606W, F775W, F850LP ACS images and F105W, F125W, F140W, and F160W WFC3/IR images. This detection image is used to derive aperture corrections, which are then applied to isophotal magnitudes measured in the UV images. The effective depth; that is, the limiting magnitude at which sources have a $> 50\%$ detection efficiency, is $m_{AB} = 27.7, 27.7, 28.2$ for F225W, F275W, and F336W, respectively.

For all individual galaxies, we determined redshifts using a Bayesian photo- z (BPZ) algorithm (Benítez 2000; Benítez et al. 2004; Coe et al. 2006), but the UVUDF catalog also includes spectroscopic redshifts, compiled by Rafelski et al. (2009) from a range of sources (Le Fèvre et al. 2004; Szokoly et al. 2004; Vanzella et al. 2005, 2006, 2008; Popesso et al. 2009). We

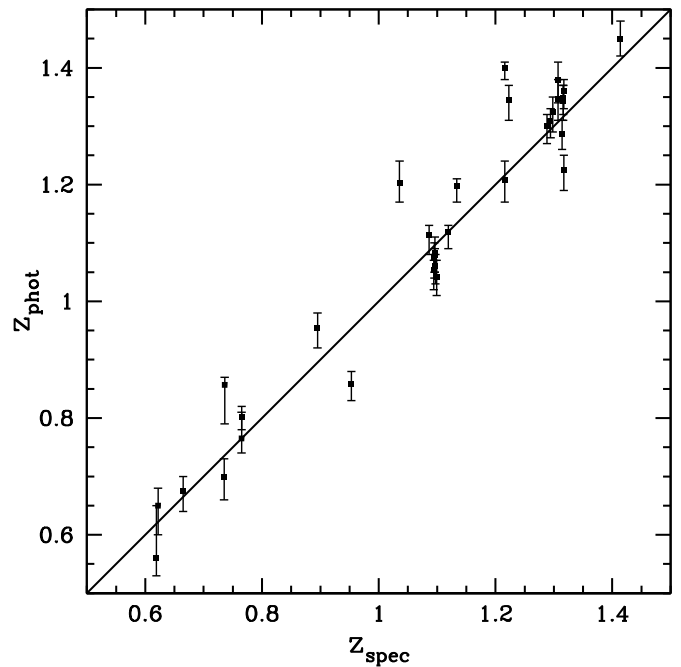


Figure 1. Photometric redshift plotted against the spectroscopic redshift for 33 galaxies in the UVUDF. The photometric redshifts have a scatter in $\Delta z/(1+z)$ of $\sigma_z = 0.030$, after excluding one 3σ outlier, and the mean has a bias of $\Delta z/(1+z) = 0.008 \pm 0.006$.

also include new measurements from Balestra et al. (2010) and Kurk et al. (2013), giving a total of 33 $0.5 < z < 1.5$ galaxies with spectroscopic redshifts. We demonstrate the accuracy of the photometric redshifts in Figure 1 by comparing them to spectroscopic redshifts for these galaxies. The photometric redshifts have a scatter in $\Delta z/(1+z)$ of $\sigma_z = 0.030$ over the range, $0.5 < z < 1.5$. In addition, there is a bias of $(z_{\text{phot}} - z_{\text{spec}})/(1+z) = 0.008 \pm 0.006$, which we find to be insignificant at $< 2\sigma$ using 1000 bootstrap simulations. We also used 125 G141 grism redshifts from the 3D-HST project (van Dokkum et al. 2013), which agree very well with the other spectroscopic redshifts, $\sigma_z = 0.0056$. For all samples here, we assume a galaxy is at its spectroscopic redshift, if one is available. If not, it is given either a grism redshift or, if no other measurement is available, a photometric redshift.

2.1. Sample Selection

We analyze two UV-luminosity-limited samples, one at $0.5 < z < 1.5$ and another at $1.5 < z < 2.5$. We select each according to the rest-frame 1500 \AA absolute magnitude, M_{1500} , which is estimated from a linear interpolation between the two nearest UV or optical magnitudes. In Figure 2, we show the distribution of M_{1500} as a function of redshift for galaxies in the UVUDF area. We implement a $M_{1500} < -17$ cut to ensure completeness at all redshifts and sufficient signal-to-noise (S/N) that concentration measurements can be made in most bandpasses (S/N per pixel > 2 , see Section 2.2 for more detail on the signal-to-noise requirements). Our source catalog is 100% complete for all galaxies brighter than this magnitude cut. The final luminosity-limited samples contain 198 galaxies at $0.5 < z < 1.5$ and 400 galaxies at $1.5 < z < 2.5$.

2.2. Structural Diagnostics

We measure galaxy sizes with a Petrosian-like radius (Petrosian 1976); specifically, the radial distance at which the

⁹ http://www.stsci.edu/hst/wfc3/tools/cte_tools

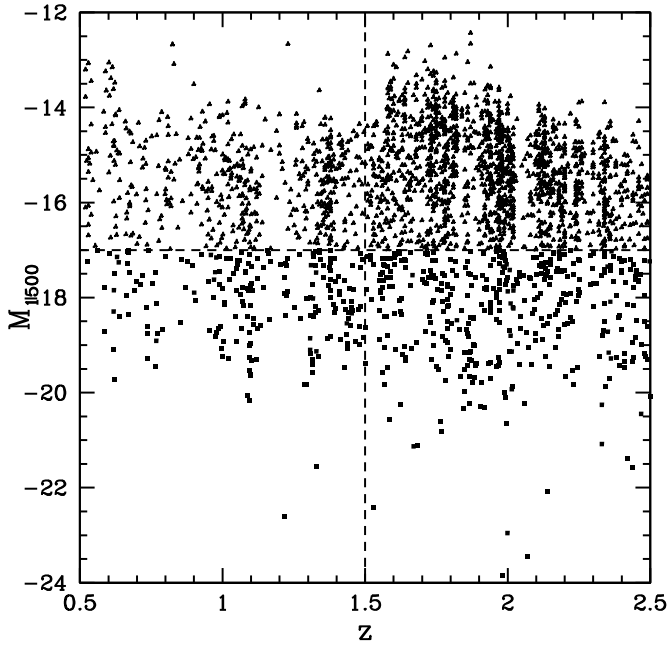


Figure 2. Distribution of absolute magnitude at 1500 Å as a function of redshift (see Section 2) for all sources in the UVUDF catalog. We separate our sample into two redshifts bins (vertical dashed line) and implement a cut at $M_{1500} < -17$ (horizontal dashed line) to ensure a sample that is luminosity-limited in the UV and for which simple morphological diagnostics can be measured (average S/N per pixel $\gtrsim 2$). Note that, at $1.5 < z < 2.5$, 1500 Å is sampled primarily by the deeper UDF optical imaging.

local surface brightness is half of the internal surface brightness, $r_{50} \equiv r(\eta = 0.5)$, and $\eta(r) \equiv I(r) / (I(< r))$. This quantity is approximately equal to the half-light radius. We define the concentration following Kent (1985) and Conselice (2003),

$$C = 5 \log \left[\frac{r_{80\%}}{r_{20\%}} \right], \quad (1)$$

where $(r_{80\%}, r_{20\%})$ are the radii at which the integrated light profile is at 80% and 20% of the light within $r(\eta = 0.2)$. Both quantities are defined in terms of a surface brightness ratio, so are insensitive to the depth of the imaging.

In order to access the rest-frame ultraviolet in $0.5 < z < 1.5$ galaxies, we use filters in the observed-frame near-UV and optical, including F225W, F275W, and F336W from the UVUDF and F435W, F606W, and F775W from the UDF. All observed-frame UV structural measurements use the peak flux in the optical/near-IR detection image as the center of the galaxy (see Section 2). We checked that our results were insensitive to the filter used to center the galaxy, alternately using the F336W and *B*-band centroids as a reference position for the structural diagnostics. No qualitative change in our results is observed. Note that in order to achieve maximum spatial resolution, we do not match the point spread functions (PSFs) between the ACS and UVIS images. The PSF in the optical ACS images is $\sim 10\%$ larger than that in the UVIS images, but most of the galaxies are well resolved and we show in Section 3 that such effects are not large enough to bias our results significantly.

In order to test the dependence of our structural diagnostics on S/N, we used object-by-object Monte Carlo simulations. To do this, we first extract the galaxies in our sample from the appropriate ACS image (nearest to $\lambda_r = 3000$ Å) using SExtractor (DETECT_MINAREA = 5 and DETECT_THRESH = 1.65). The ACS images are much deeper than the corresponding WFC3

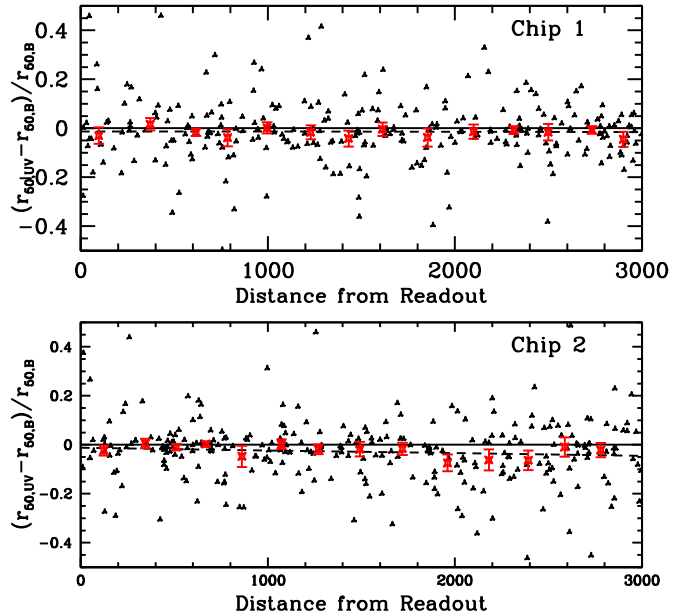


Figure 3. Fractional difference in r_{50} as a function of distance from the CCD readout for UVIS Chip 1 (top) and UVIS Chip 2 (bottom). Black triangles indicate individual galaxies, while red squares indicate the median differential radius in 10 object bins. Each panel includes a linear least squares fit (dashed line) to the data, both of which are consistent with the zero line (solid line) at $< 1.5\sigma$. If the CTI were having a significant impact on the r_{50} measurements, we would expect them to systematically decrease approaching the readout. No such effect is observed.

(A color version of this figure is available in the online journal.)

observations, and are therefore a good approximation of the galaxy’s “true” light distribution. We then simulated a noise-free WFC3 UVIS observation by normalizing this cutout so that the object’s aperture-corrected magnitude is the same as that in the real UV image. Noise was then added using actual realizations from blank regions in the epoch 3 WFC3 image. We find that there are systematic decreases in both r_e and C at very low S/N, but these decreases are $< 1\%$ when the average S/N pixel is $\gtrsim 2$ within a 1 pixel annulus centered at $r(\eta = 0.5)$ and $r_{80\%}$, respectively. As such, we restrict our analyses in the UV to objects brighter than this limit.

2.3. Charge Transfer Inefficiency

One of the downsides to space-based CCD imaging is that the cumulative damage from cosmic radiation, in the form of charged particles, can create “charge traps” in the detector. When charge is transferred across the CCD in the readout phase, it can get caught in these traps, leading to a systematic loss of source flux in the processed image, as well as the creation of trails as the charge is eventually released later in the readout phase. This CTI is especially problematic in UV images, where the sky background is low and the majority of the trapped charges will be from individually detected sources. In galaxies detected at moderate-to-high S/N, the CTI effects can be corrected, but sources at the faint end can be lost entirely due to these effects. The impact of CTI on galaxy shape measurements has been studied in the context of weak lensing (Rhodes et al. 2010), and it was found that galaxies far from the CCD readout can have their ellipticities altered by CTI effects.

For a detailed discussion of the impact of CTI on the UVUDF images and catalog, see Teplitz et al. (2013). In Figure 3, we plot the fractional difference in r_{50} as a function of distance from the CCD readout in the UVUDF observations. Each panel includes

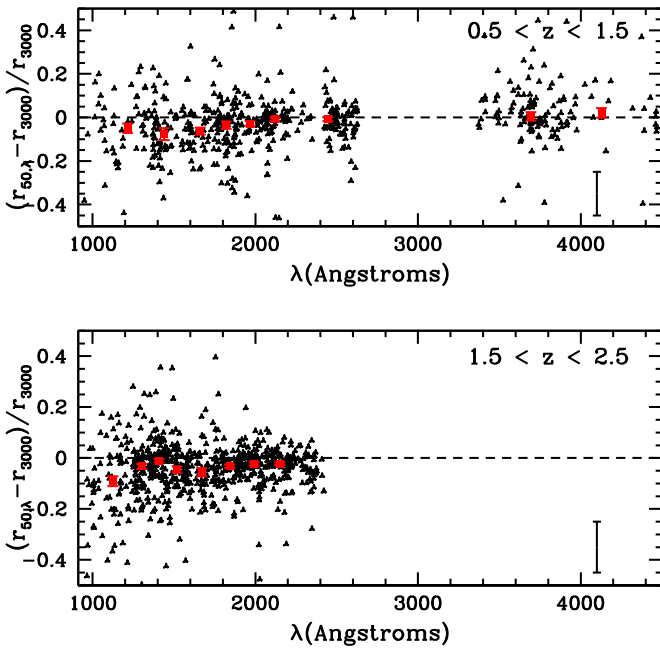


Figure 4. Difference in r_{50} as a function of rest-frame wavelength for a sample of 198 $0.5 < z < 1.5$ galaxies with $M_{1500} < -17$ (top) and a sample of 400 $1.5 < z < 2.5$ galaxies with the same magnitude cutoff (bottom). Differences are taken relative to the filter nearest to rest-frame 3000 Å. Black triangles indicate individual measurements, while red squares indicate the median differential radius in 10 object bins. Error bars for the medians are derived from 1000 bootstrap simulations and a typical error bar for the individual measurements is given in the lower right corner. The median r_{50} exhibits a decrease at the bluest wavelengths, but remains constant to $<15\%$ over the range, $1200 < \lambda_r < 4000$ Å.

(A color version of this figure is available in the online journal.)

a linear least squares fit to the data (dashed line), both with slopes and y-intercepts that are consistent with zero at $<1.5\sigma$. We therefore infer that there is no systematic change in r_{50} as a function of distance from the readout, as one might expect if CTI effects were significant. Note that both the post-flash and the pixel-by-pixel CTI correction mitigate the effects of the CTI in these observations.

3. WAVELENGTH DEPENDENCE OF r_{50} AND CONCENTRATION

Ultraviolet light in the rest frame of galaxies will be dominated by recent ($\lesssim 100$ Myr) star formation, but observing bluer UV light allows us to distinguish the youngest (~ 10 Myr) star formation, as well as regions least extinguished by dust. By analyzing the wavelength dependence of simple structural diagnostics, such as r_{50} and concentration, we can characterize the spatial variation of these changes. In Table 1, we give the position, photometric redshift, M_{1500} , r_{50} at 3000 Å (r_{3000}), and C at 3000 Å (C_{3000}) for each galaxy in the $0.5 < z < 1.5$ sample.

In the top panel of Figure 4, we show how r_{50} depends upon rest-frame wavelength in our sample of $0.5 < z < 1.5$ galaxies. For each galaxy, we plot the fractional difference in r_{50} relative to the filter nearest to rest-frame 3000 Å. This choice of wavelength ensures that the reference measurement is taken in the observed-frame optical UDF images, in which all of our galaxies are detected at high S/N. The reader should bear in mind that our observations use broadband filters, with typical widths at $z \sim 1$ ranging from $\Delta\lambda_r \sim 200$ Å at 1000 Å to $\Delta\lambda_r \sim 1000$ Å at

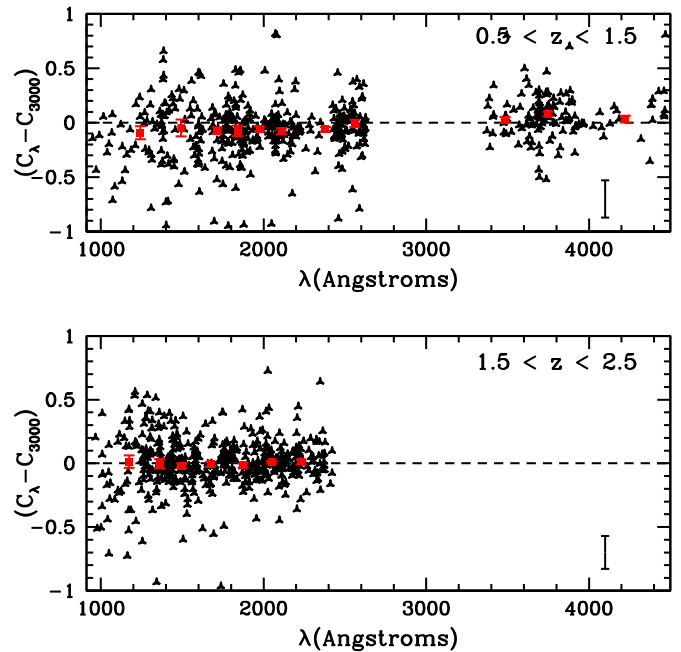


Figure 5. Same as Figure 4, except we plot the difference in concentration. (A color version of this figure is available in the online journal.)

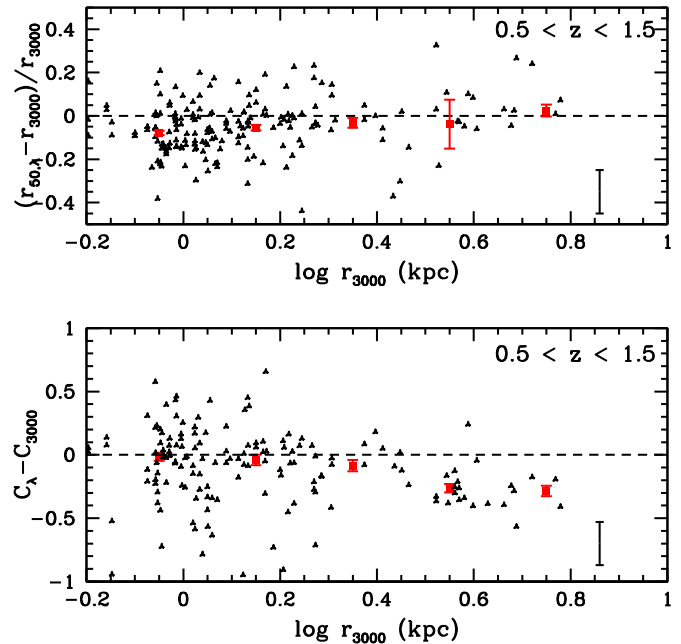


Figure 6. Difference in r_{50} (top panel) and concentration (bottom panel) as a function of r_{3000} for a sample of $0.5 < z < 1.5$ galaxies with $M_{1500} < -17$. Differences are taken between far-UV wavelengths, $\lambda_r < 1800$ Å, and the filter nearest to rest-frame 3000 Å. Black triangles indicate individual measurements, while red square points indicate the median differential radius in bins of $\Delta \log r_{3000} = 0.2$. Error bars for the medians are derived from 1000 bootstrap simulations and a typical error bar for the individual measurements is given in the lower right corner. The fractional difference in r_{50} is independent of size, while large galaxies are systematically less concentrated in the far-UV than the near-UV. This is likely due to the presence of bulges in many of the larger objects, which are faint at the bluest wavelengths.

(A color version of this figure is available in the online journal.)

4000 Å. Measurements near 912 Å, for example, will include light both blueward and redward of the Lyman break.

As shown in Figure 4, the median r_{50} decreases at $\lambda < 1800$ Å for galaxies in both redshift intervals. When we consider only

Table 1
Galaxy Samples

Number ^a	α^b	δ^b	z	M_{1500}^c	r_{3000}^d (")	C_{3000}^e
1267	3:32:38.522	-27:48:38.327	1.341	-17.05 ± 0.12	0.119 ± 0.005	2.22 ± 0.08
1269	3:32:38.608	-27:48:37.577	1.425	-17.90 ± 0.09	0.157 ± 0.007	2.50 ± 0.09
1478	3:32:38.397	-27:48:28.997	1.489	-18.20 ± 0.08	0.441 ± 0.016	2.55 ± 0.12
1481	3:32:39.982	-27:48:30.610	0.959	-17.10 ± 0.12	0.189 ± 0.007	2.56 ± 0.10
1531	3:32:37.751	-27:48:30.170	1.496	-17.20 ± 0.12	0.219 ± 0.019	3.00 ± 0.14
1626	3:32:38.352	-27:48:25.728	1.458	-18.30 ± 0.08	0.517 ± 0.019	2.01 ± 0.11
1668	3:32:40.482	-27:48:26.558	1.167	-18.47 ± 0.07	0.129 ± 0.003	2.67 ± 0.07
1693	3:32:37.877	-27:48:26.719	1.120	-17.01 ± 0.13	0.130 ± 0.006	2.67 ± 0.09
1752	3:32:40.923	-27:48:24.006	1.470	-18.81 ± 0.05	0.098 ± 0.002	3.82 ± 0.08
1829	3:32:40.927	-27:48:23.646	1.298	-18.36 ± 0.07	0.165 ± 0.004	2.73 ± 0.07
1960	3:32:35.964	-27:48:11.906	0.605	-17.07 ± 0.12	0.129 ± 0.001	3.76 ± 0.04
2322	3:32:39.111	-27:48:01.844	1.270	-18.27 ± 0.07	0.102 ± 0.003	2.49 ± 0.07
2333	3:32:36.853	-27:48:13.103	1.310	-17.32 ± 0.11	0.237 ± 0.011	2.39 ± 0.10
2461	3:32:41.587	-27:48:08.252	1.123	-17.18 ± 0.12	0.150 ± 0.008	3.04 ± 0.11
2763	3:32:36.613	-27:48:01.254	1.492	-18.64 ± 0.06	0.335 ± 0.009	3.03 ± 0.11
2934	3:32:37.696	-27:48:02.420	1.143	-17.37 ± 0.11	0.110 ± 0.004	2.45 ± 0.07
2998	3:32:36.287	-27:47:55.285	0.713	-17.73 ± 0.10	0.361 ± 0.005	2.33 ± 0.07
3031	3:32:36.387	-27:47:58.585	1.439	-18.97 ± 0.05	0.474 ± 0.015	2.55 ± 0.11
3123	3:32:42.948	-27:47:55.134	1.065	-18.08 ± 0.08	0.185 ± 0.004	2.95 ± 0.08
3180	3:32:37.879	-27:47:51.079	0.768	-18.91 ± 0.05	0.336 ± 0.006	2.56 ± 0.10
3243	3:32:38.648	-27:47:56.206	1.355	-17.59 ± 0.11	0.367 ± 0.016	2.48 ± 0.12
3257	3:32:38.955	-27:47:55.095	1.379	-17.99 ± 0.09	0.501 ± 0.026	2.16 ± 0.12
3270	3:32:38.670	-27:47:55.696	1.229	-17.86 ± 0.09	0.255 ± 0.011	3.07 ± 0.12
3349	3:32:41.675	-27:47:50.462	0.668	-17.29 ± 0.12	0.500 ± 0.008	2.63 ± 0.09
3372	3:32:42.247	-27:47:46.139	0.794	-18.69 ± 0.07	0.734 ± 0.004	2.68 ± 0.08
3373	3:32:40.049	-27:47:51.790	0.995	-18.60 ± 0.07	0.449 ± 0.007	2.02 ± 0.08
3613	3:32:37.632	-27:47:44.300	1.097	-19.62 ± 0.02	0.410 ± 0.004	2.76 ± 0.07
3655	3:32:37.567	-27:47:50.181	1.327	-17.03 ± 0.12	0.110 ± 0.005	2.45 ± 0.08
3677	3:32:37.309	-27:47:29.362	0.669	-18.35 ± 0.07	0.270 ± 0.001	3.37 ± 0.06
3752	3:32:43.246	-27:47:44.003	1.440	-18.28 ± 0.07	0.154 ± 0.008	3.04 ± 0.10
3799	3:32:38.353	-27:47:44.418	1.442	-18.31 ± 0.08	0.710 ± 0.031	2.14 ± 0.13
3977	3:32:37.397	-27:47:41.601	1.095	-19.26 ± 0.04	0.555 ± 0.007	2.65 ± 0.08
4052	3:32:40.632	-27:47:39.997	1.040	-17.50 ± 0.11	0.240 ± 0.008	2.94 ± 0.11
4094	3:32:37.594	-27:47:39.531	0.663	-17.96 ± 0.09	0.136 ± 0.005	3.98 ± 0.12
4142	3:32:44.197	-27:47:33.527	0.737	-19.28 ± 0.03	0.240 ± 0.001	2.79 ± 0.02
4253	3:32:39.888	-27:47:38.261	1.049	-18.92 ± 0.05	0.459 ± 0.010	2.39 ± 0.10
4332	3:32:33.456	-27:47:39.512	1.403	-17.92 ± 0.09	0.131 ± 0.004	2.57 ± 0.07
4396	3:32:35.796	-27:47:34.736	1.223	-17.97 ± 0.09	0.145 ± 0.005	3.19 ± 0.10
4438	3:32:33.031	-27:47:30.633	0.977	-18.82 ± 0.06	0.700 ± 0.007	2.31 ± 0.09
4458	3:32:36.054	-27:47:37.796	1.340	-21.47 ± 0.06	0.132 ± 0.017	1.13 ± 0.13
4481	3:32:39.264	-27:47:36.704	1.367	-18.87 ± 0.05	0.187 ± 0.004	2.87 ± 0.07
4491	3:32:40.216	-27:47:32.979	1.095	-19.53 ± 0.03	0.578 ± 0.006	2.69 ± 0.08
4587	3:32:40.673	-27:47:30.997	0.667	-17.02 ± 0.13	0.266 ± 0.001	2.75 ± 0.04
4591	3:32:41.120	-27:47:34.595	1.009	-18.13 ± 0.08	0.410 ± 0.009	2.87 ± 0.10
4616	3:32:42.737	-27:47:33.986	1.427	-17.63 ± 0.11	0.435 ± 0.022	2.46 ± 0.13
4662	3:32:39.490	-27:47:34.663	1.098	-17.69 ± 0.10	0.221 ± 0.009	3.10 ± 0.11
4767	3:32:40.607	-27:47:30.247	0.669	-17.01 ± 0.15	1.384 ± 0.010	1.15 ± 0.09
4816	3:32:44.165	-27:47:29.447	1.220	-18.37 ± 0.07	0.198 ± 0.004	3.29 ± 0.09
4835	3:32:34.867	-27:47:30.689	1.317	-18.02 ± 0.08	0.188 ± 0.006	2.97 ± 0.10
4849	3:32:39.321	-27:47:32.174	1.379	-17.42 ± 0.11	0.165 ± 0.009	2.50 ± 0.10
4976	3:32:34.693	-27:47:28.019	1.466	-18.93 ± 0.05	0.186 ± 0.004	3.12 ± 0.10
4981	3:32:34.659	-27:47:28.019	1.438	-19.06 ± 0.04	0.157 ± 0.003	2.91 ± 0.08
4999	3:32:36.352	-27:47:27.985	1.378	-18.82 ± 0.05	0.215 ± 0.008	3.48 ± 0.11
5115	3:32:32.651	-27:47:27.333	1.355	-17.33 ± 0.11	0.136 ± 0.011	3.61 ± 0.13
5187	3:32:44.355	-27:47:23.776	0.953	-17.66 ± 0.10	0.163 ± 0.002	2.77 ± 0.06
5190	3:32:34.808	-27:47:21.839	1.316	-19.59 ± 0.03	0.443 ± 0.005	2.49 ± 0.08
5216	3:32:34.261	-27:47:24.090	1.098	-18.16 ± 0.09	0.570 ± 0.018	1.73 ± 0.11
5268	3:32:40.324	-27:47:22.809	0.619	-17.85 ± 0.10	0.336 ± 0.003	2.26 ± 0.06
5388	3:32:41.857	-27:47:21.901	1.325	-18.32 ± 0.08	0.368 ± 0.010	2.76 ± 0.10
5417	3:32:39.881	-27:47:15.011	1.095	-20.17 ± 0.01	0.935 ± 0.005	2.02 ± 0.08
5497	3:32:37.763	-27:47:21.200	1.092	-17.28 ± 0.12	0.284 ± 0.011	2.31 ± 0.10
5569	3:32:35.328	-27:47:18.478	0.674	-17.47 ± 0.11	0.273 ± 0.003	2.76 ± 0.06
5658	3:32:41.766	-27:47:16.831	1.096	-18.74 ± 0.06	0.272 ± 0.007	3.78 ± 0.11
5661	3:32:31.776	-27:47:20.194	1.412	-17.55 ± 0.10	0.178 ± 0.009	2.37 ± 0.10

Table 1
(Continued)

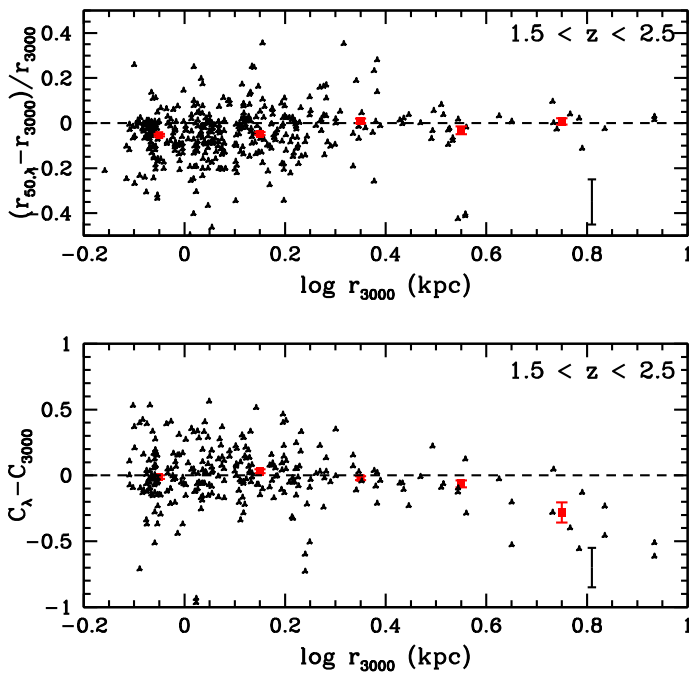
Number ^a	α^b	δ^b	z	M_{1500}^c	r_{3000}^d (")	C_{3000}^e
5694	3:32:43.475	-27:47:12.921	1.095	-19.01 ± 0.05	0.630 ± 0.012	2.55 ± 0.11
5709	3:32:35.667	-27:47:19.137	1.221	-17.28 ± 0.11	0.104 ± 0.005	2.49 ± 0.08
5753	3:32:32.328	-27:47:18.364	1.027	-17.17 ± 0.12	0.194 ± 0.010	3.06 ± 0.11
5896	3:32:36.958	-27:47:15.773	1.123	-17.59 ± 0.10	0.141 ± 0.004	3.08 ± 0.09
5898	3:32:31.397	-27:47:13.085	1.479	-18.26 ± 0.08	0.351 ± 0.014	3.06 ± 0.12
5922	3:32:31.568	-27:47:11.164	1.008	-18.10 ± 0.09	0.522 ± 0.017	2.60 ± 0.12
5959	3:32:39.381	-27:47:14.263	1.109	-18.43 ± 0.07	0.122 ± 0.002	2.42 ± 0.04
5975	3:32:41.692	-27:47:13.562	1.450	-18.58 ± 0.06	0.204 ± 0.006	2.71 ± 0.09
5989	3:32:38.633	-27:47:11.356	1.134	-18.59 ± 0.07	0.395 ± 0.007	2.44 ± 0.08
5995	3:32:42.662	-27:47:13.106	0.968	-17.99 ± 0.09	0.217 ± 0.005	2.71 ± 0.09
6022	3:32:35.310	-27:47:13.588	1.392	-18.30 ± 0.07	0.116 ± 0.002	2.73 ± 0.06
6027	3:32:39.637	-27:47:09.132	1.317	-17.07 ± 0.12	0.129 ± 0.004	3.93 ± 0.12
6079	3:32:33.458	-27:47:12.392	1.298	-18.02 ± 0.09	0.226 ± 0.006	2.84 ± 0.09
6107	3:32:39.838	-27:47:11.861	1.081	-17.49 ± 0.11	0.271 ± 0.012	2.36 ± 0.10
6118	3:32:43.498	-27:47:11.931	1.090	-17.86 ± 0.09	0.187 ± 0.007	2.28 ± 0.13
6153	3:32:34.941	-27:47:10.169	1.380	-17.18 ± 0.12	0.126 ± 0.009	2.41 ± 0.12
6187	3:32:37.480	-27:47:10.491	0.980	-17.16 ± 0.12	0.230 ± 0.011	2.54 ± 0.10
6196	3:32:38.513	-27:47:10.667	0.990	-17.73 ± 0.10	0.131 ± 0.003	2.56 ± 0.06
6235	3:32:34.907	-27:47:10.439	1.380	-17.63 ± 0.10	0.150 ± 0.011	2.68 ± 0.13
6583	3:32:36.447	-27:47:05.094	1.224	-17.33 ± 0.11	0.126 ± 0.006	2.46 ± 0.08
6627	3:32:35.384	-27:47:04.258	0.989	-17.46 ± 0.11	0.122 ± 0.004	2.51 ± 0.07
6645	3:32:33.176	-27:47:03.842	1.326	-18.18 ± 0.08	0.498 ± 0.017	2.21 ± 0.11
6673	3:32:34.767	-27:47:04.379	1.272	-17.08 ± 0.12	0.116 ± 0.006	2.39 ± 0.08
6710	3:32:46.235	-27:47:01.682	0.980	-17.64 ± 0.10	0.244 ± 0.009	3.57 ± 0.12
6754	3:32:31.292	-27:47:02.375	1.093	-17.82 ± 0.09	0.148 ± 0.004	2.92 ± 0.09
6782	3:32:32.506	-27:47:01.983	1.446	-17.81 ± 0.09	0.156 ± 0.006	2.38 ± 0.09
6785	3:32:45.966	-27:46:57.754	1.331	-19.24 ± 0.05	0.972 ± 0.013	2.38 ± 0.10
6821	3:32:42.774	-27:46:59.066	1.119	-19.30 ± 0.04	0.445 ± 0.004	2.12 ± 0.07
6846	3:32:44.298	-27:47:00.016	1.143	-17.78 ± 0.09	0.108 ± 0.003	2.86 ± 0.07
6853	3:32:36.435	-27:46:58.344	0.852	-18.51 ± 0.06	0.150 ± 0.002	2.87 ± 0.05
6862	3:32:41.422	-27:46:51.453	0.620	-17.49 ± 0.11	0.584 ± 0.004	2.56 ± 0.08
6886	3:32:43.497	-27:46:59.091	1.400	-18.23 ± 0.08	0.185 ± 0.006	3.20 ± 0.10
6894	3:32:31.132	-27:47:00.305	1.160	-17.00 ± 0.13	0.122 ± 0.005	2.52 ± 0.08
6922	3:32:36.178	-27:46:57.265	1.315	-17.72 ± 0.11	0.808 ± 0.040	2.86 ± 0.14
6933	3:32:33.429	-27:46:50.462	0.735	-18.21 ± 0.08	0.547 ± 0.006	2.41 ± 0.09
6939	3:32:46.068	-27:46:58.713	1.050	-17.39 ± 0.11	0.345 ± 0.011	2.03 ± 0.10
6949	3:32:44.239	-27:47:00.136	1.379	-17.25 ± 0.11	0.114 ± 0.007	2.53 ± 0.09
6953	3:32:36.668	-27:46:57.684	0.765	-17.48 ± 0.11	0.183 ± 0.004	2.51 ± 0.07
6957	3:32:35.063	-27:46:58.738	1.441	-18.44 ± 0.07	0.217 ± 0.005	2.36 ± 0.08
6974	3:32:37.954	-27:46:51.919	0.620	-19.10 ± 0.05	0.839 ± 0.004	2.11 ± 0.07
7036	3:32:45.681	-27:46:55.206	1.317	-19.30 ± 0.03	0.155 ± 0.003	3.30 ± 0.09
7067	3:32:32.443	-27:46:56.403	1.454	-18.33 ± 0.07	0.191 ± 0.005	2.87 ± 0.09
7071	3:32:36.442	-27:46:55.134	0.900	-17.90 ± 0.09	0.386 ± 0.006	2.74 ± 0.10
7081	3:32:38.958	-27:46:56.325	1.436	-18.54 ± 0.07	0.674 ± 0.013	1.61 ± 0.10
7112	3:32:39.815	-27:46:53.531	1.110	-18.57 ± 0.07	0.409 ± 0.005	1.64 ± 0.07
7131	3:32:32.459	-27:46:54.033	1.451	-18.22 ± 0.08	0.124 ± 0.002	2.80 ± 0.06
7136	3:32:38.990	-27:46:56.715	1.429	-17.65 ± 0.10	0.108 ± 0.005	2.33 ± 0.12
7193	3:32:33.429	-27:46:55.382	1.456	-17.32 ± 0.11	0.190 ± 0.015	2.52 ± 0.12
7269	3:32:41.890	-27:46:51.271	0.734	-17.58 ± 0.11	0.464 ± 0.009	3.29 ± 0.11
7290	3:32:36.928	-27:46:53.993	1.229	-17.17 ± 0.12	0.143 ± 0.008	2.46 ± 0.09
7370	3:32:32.712	-27:46:51.543	1.451	-18.09 ± 0.08	0.121 ± 0.003	2.65 ± 0.07
7394	3:32:38.990	-27:46:51.045	1.372	-17.75 ± 0.09	0.104 ± 0.003	2.40 ± 0.07
7398	3:32:42.319	-27:46:51.088	0.631	-17.15 ± 0.12	0.107 ± 0.002	2.59 ± 0.05
7452	3:32:44.189	-27:46:46.967	0.670	-17.02 ± 0.13	0.270 ± 0.006	2.83 ± 0.10
7556	3:32:40.781	-27:46:15.757	0.622	-19.72 ± 0.04	1.288 ± 0.007	2.50 ± 0.09
7559	3:32:38.100	-27:46:13.849	0.998	-19.07 ± 0.05	0.498 ± 0.004	2.12 ± 0.07
7647	3:32:41.425	-27:46:15.093	1.010	-17.17 ± 0.12	0.334 ± 0.016	3.18 ± 0.13
7664	3:32:36.954	-27:46:15.563	0.865	-17.76 ± 0.10	0.402 ± 0.009	3.02 ± 0.11
7678	3:32:38.986	-27:46:15.225	1.049	-17.84 ± 0.09	0.251 ± 0.006	2.90 ± 0.10
7705	3:32:37.563	-27:46:46.761	1.337	-18.28 ± 0.08	0.264 ± 0.012	2.80 ± 0.12
7725	3:32:35.078	-27:46:15.658	1.316	-19.40 ± 0.04	0.626 ± 0.009	2.17 ± 0.09
7756	3:32:33.926	-27:46:16.861	1.492	-17.79 ± 0.10	0.372 ± 0.016	2.72 ± 0.12
7786	3:32:37.065	-27:46:17.122	1.274	-18.44 ± 0.07	0.157 ± 0.002	3.46 ± 0.07
7889	3:32:44.274	-27:46:20.116	0.877	-17.23 ± 0.12	0.224 ± 0.008	3.19 ± 0.11

Table 1
(Continued)

Number ^a	α^b	δ^b	z	M_{1500}^c	r_{3000}^d (")	C_{3000}^e
7959	3:32:34.758	-27:46:42.929	1.484	-17.37 ± 0.11	0.132 ± 0.006	2.67 ± 0.09
7974	3:32:37.728	-27:46:42.620	1.307	-19.10 ± 0.04	0.209 ± 0.003	2.76 ± 0.07
7995	3:32:42.253	-27:46:25.289	1.288	-19.82 ± 0.02	0.731 ± 0.008	1.71 ± 0.09
8051	3:32:37.425	-27:46:22.491	1.106	-17.85 ± 0.09	0.209 ± 0.006	2.89 ± 0.10
8125	3:32:41.514	-27:46:40.353	1.102	-19.32 ± 0.04	0.451 ± 0.006	2.78 ± 0.09
8242	3:32:34.954	-27:46:24.329	1.100	-17.33 ± 0.11	0.122 ± 0.004	2.34 ± 0.07
8255	3:32:34.627	-27:46:37.799	1.101	-17.35 ± 0.11	0.135 ± 0.004	2.92 ± 0.09
8257	3:32:38.596	-27:46:31.277	0.618	-18.29 ± 0.09	0.913 ± 0.005	2.44 ± 0.08
8270	3:32:43.971	-27:46:32.448	0.980	-18.73 ± 0.06	0.409 ± 0.006	2.51 ± 0.08
8275	3:32:36.451	-27:46:28.164	0.772	-18.76 ± 0.05	0.142 ± 0.002	2.51 ± 0.09
8314	3:32:36.661	-27:46:31.014	0.999	-17.81 ± 0.09	0.254 ± 0.005	3.19 ± 0.09
8316	3:32:38.300	-27:46:28.458	1.122	-18.65 ± 0.06	0.186 ± 0.010	3.27 ± 0.12
8372	3:32:35.619	-27:46:32.847	0.586	-17.78 ± 0.10	0.466 ± 0.004	2.93 ± 0.08
8374	3:32:35.391	-27:46:30.507	1.069	-17.06 ± 0.12	0.154 ± 0.008	2.52 ± 0.09
8392	3:32:34.186	-27:46:34.620	1.376	-17.36 ± 0.11	0.174 ± 0.007	2.53 ± 0.09
8461	3:32:44.618	-27:46:32.174	1.426	-19.46 ± 0.04	0.673 ± 0.009	1.83 ± 0.09
8501	3:32:44.747	-27:46:37.303	1.377	-17.01 ± 0.13	0.159 ± 0.010	2.43 ± 0.10
8551	3:32:36.403	-27:46:31.375	1.018	-19.27 ± 0.04	0.339 ± 0.005	2.85 ± 0.09
8585	3:32:35.485	-27:46:27.297	1.099	-19.64 ± 0.02	0.230 ± 0.002	3.39 ± 0.09
8597	3:32:41.860	-27:46:34.471	1.485	-17.08 ± 0.12	0.180 ± 0.014	2.31 ± 0.12
8653	3:32:39.220	-27:46:36.104	1.319	-18.40 ± 0.07	0.134 ± 0.003	2.58 ± 0.07
8680	3:32:35.465	-27:46:36.987	1.086	-18.40 ± 0.07	0.162 ± 0.002	2.59 ± 0.06
8693	3:32:44.358	-27:46:38.866	0.524	-17.23 ± 0.12	0.570 ± 0.008	3.99 ± 0.12
8744	3:32:35.192	-27:46:38.968	1.080	-17.44 ± 0.11	0.137 ± 0.004	2.34 ± 0.07
8749	3:32:34.857	-27:46:40.469	1.099	-17.75 ± 0.10	0.403 ± 0.005	2.04 ± 0.08
8765	3:32:36.562	-27:46:40.614	1.414	-18.89 ± 0.05	0.296 ± 0.006	2.37 ± 0.08
8776	3:32:36.589	-27:46:39.714	1.425	-18.08 ± 0.08	0.110 ± 0.004	2.59 ± 0.08
8801	3:32:41.510	-27:46:42.183	1.308	-18.00 ± 0.09	0.518 ± 0.021	2.54 ± 0.12
8810	3:32:37.266	-27:46:10.342	0.736	-18.75 ± 0.06	0.501 ± 0.003	2.09 ± 0.06
8872	3:32:43.038	-27:46:43.974	1.343	-17.19 ± 0.12	0.156 ± 0.016	2.96 ± 0.13
8930	3:32:37.500	-27:46:45.351	1.270	-17.67 ± 0.10	0.167 ± 0.013	2.82 ± 0.12
8941	3:32:37.644	-27:46:41.810	1.317	-17.14 ± 0.12	0.121 ± 0.006	2.43 ± 0.09
9018	3:32:35.296	-27:46:42.328	1.098	-18.96 ± 0.05	0.495 ± 0.007	2.18 ± 0.09
9090	3:32:39.350	-27:46:09.673	1.378	-17.85 ± 0.09	0.188 ± 0.013	1.82 ± 0.14
9125	3:32:39.915	-27:46:06.911	1.294	-19.82 ± 0.02	0.707 ± 0.009	2.06 ± 0.09
9183	3:32:38.446	-27:46:09.527	1.064	-18.65 ± 0.06	0.448 ± 0.009	2.33 ± 0.10
9244	3:32:38.760	-27:46:03.496	0.690	-17.85 ± 0.09	0.149 ± 0.002	2.72 ± 0.05
9253	3:32:42.813	-27:46:05.635	0.676	-19.62 ± 0.03	0.874 ± 0.003	2.65 ± 0.06
9264	3:32:37.192	-27:46:08.062	1.096	-17.82 ± 0.09	0.191 ± 0.002	3.53 ± 0.08
9273	3:32:40.162	-27:46:05.680	1.068	-17.79 ± 0.10	0.403 ± 0.021	2.07 ± 0.12
9332	3:32:43.120	-27:46:07.553	1.486	-18.99 ± 0.05	0.492 ± 0.010	2.93 ± 0.10
9341	3:32:38.365	-27:46:00.618	1.046	-18.40 ± 0.07	0.395 ± 0.008	2.35 ± 0.10
9348	3:32:36.871	-27:46:04.013	0.640	-17.27 ± 0.11	0.140 ± 0.004	3.63 ± 0.11
9402	3:32:35.056	-27:45:59.698	0.954	-18.69 ± 0.06	0.341 ± 0.007	2.92 ± 0.10
9437	3:32:35.806	-27:45:49.046	0.738	-18.61 ± 0.07	0.759 ± 0.007	2.48 ± 0.08
9444	3:32:37.298	-27:45:57.892	1.096	-17.10 ± 0.13	0.376 ± 0.008	2.67 ± 0.10
9455	3:32:41.334	-27:45:54.454	0.581	-18.69 ± 0.06	0.519 ± 0.005	2.90 ± 0.09
9474	3:32:39.467	-27:45:57.073	1.065	-17.93 ± 0.09	0.445 ± 0.010	1.75 ± 0.10
9532	3:32:36.330	-27:46:00.055	0.895	-17.33 ± 0.11	0.164 ± 0.003	3.01 ± 0.07
9649	3:32:40.198	-27:46:02.859	1.052	-17.21 ± 0.12	0.426 ± 0.018	2.64 ± 0.11
9672	3:32:37.851	-27:45:22.370	0.925	-17.09 ± 0.12	0.156 ± 0.006	3.16 ± 0.10
9712	3:32:37.887	-27:45:18.769	0.906	-18.07 ± 0.08	0.157 ± 0.002	2.64 ± 0.06
9759	3:32:38.330	-27:45:44.208	1.337	-19.23 ± 0.04	0.644 ± 0.014	2.06 ± 0.11
9765	3:32:36.328	-27:45:41.035	0.978	-17.48 ± 0.11	0.255 ± 0.007	2.37 ± 0.09
9783	3:32:37.349	-27:45:37.821	1.390	-17.16 ± 0.12	0.129 ± 0.008	2.97 ± 0.11
9837	3:32:36.676	-27:45:39.144	1.061	-17.22 ± 0.12	0.279 ± 0.011	3.04 ± 0.11
9868	3:32:39.322	-27:45:32.924	1.150	-17.02 ± 0.13	0.344 ± 0.011	2.01 ± 0.10
9962	3:32:37.496	-27:45:26.631	0.858	-17.20 ± 0.12	0.159 ± 0.003	2.74 ± 0.07
9974	3:32:38.093	-27:45:26.839	1.025	-17.62 ± 0.11	0.504 ± 0.015	2.50 ± 0.11
9980	3:32:37.268	-27:45:28.192	1.170	-17.24 ± 0.12	0.119 ± 0.006	2.36 ± 0.08
20037	3:32:38.245	-27:46:30.078	1.216	-17.92 ± 0.09	0.184 ± 0.004	2.56 ± 0.08
56612	3:32:36.405	-27:45:40.645	1.004	-18.92 ± 0.05	0.122 ± 0.001	2.39 ± 0.03
56720	3:32:35.772	-27:45:48.596	0.699	-17.65 ± 0.10	0.261 ± 0.004	2.82 ± 0.10
56815	3:32:36.197	-27:45:36.565	0.562	-17.01 ± 0.13	0.561 ± 0.005	3.20 ± 0.10

Table 1
(Continued)

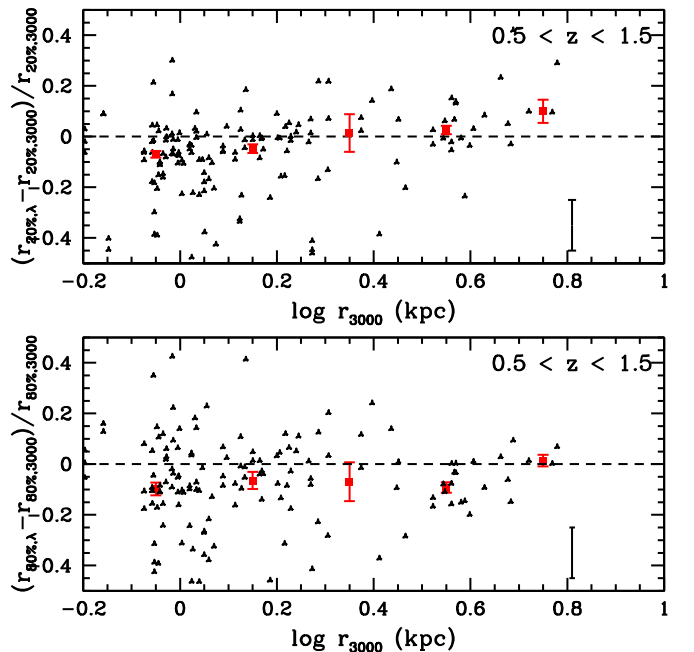
Number ^a	α^b	δ^b	z	M_{1500}^c	r_{3000}^d (")	C_{3000}^e
56986	3:32:30.420	-27:46:57.275	1.439	-18.80 ± 0.05	0.162 ± 0.003	2.68 ± 0.07
57344	3:32:47.279	-27:46:50.154	0.678	-17.08 ± 0.12	0.185 ± 0.003	2.52 ± 0.06
57390	3:32:30.949	-27:46:49.565	1.050	-17.30 ± 0.11	0.118 ± 0.008	2.39 ± 0.11
57616	3:32:34.909	-27:46:00.389	1.285	-17.99 ± 0.09	0.253 ± 0.011	2.98 ± 0.12
58728	3:32:32.741	-27:46:30.003	1.307	-18.86 ± 0.05	0.209 ± 0.003	2.44 ± 0.07
60189	3:32:38.153	-27:45:13.398	0.768	-18.13 ± 0.08	0.370 ± 0.004	3.16 ± 0.08

Notes.^a Index in Coe et al. (2006).^b Position based on an optical+IR detection image (M. Rafelski et al., in preparation).^c 1500 Å rest-frame absolute magnitude.^d Petrosian-like half-light radius at rest-frame 3000 Å.^e Concentration parameter at rest-frame 3000 Å.**Figure 7.** Same as Figure 6, but for the $1.5 < z < 2.5$ sample. There is no evidence for a systematic decrease in concentration except for galaxies with $r_{3000} \gtrsim 4$ kpc.

(A color version of this figure is available in the online journal.)

points bluer than this wavelength, the median change in r_{50} is $5.5\% \pm 0.9\%$, while averaging over all $\lambda < 3000$ Å yields a change of $3.0\% \pm 0.5\%$. At $z \sim 2$, the same measurements give a decrease in r_{50} of $3.7\% \pm 0.6\%$ and $3.2\% \pm 0.3\%$. The concentration, shown in Figure 5, also decreases at $z \sim 1$ for $\lambda < 1800$ Å, with $\Delta C = -0.07 \pm 0.02$ at $z \sim 1$ ($\Delta C = -0.06 \pm 0.01$ for $\lambda < 3000$ Å). This is not consistent with the change in concentration seen at $z \sim 2$ ($\Delta C = -0.01 \pm 0.01$ for $\lambda < 1800$ Å), suggesting that the wavelength dependence of concentration is more substantial at low redshift.

We also plot the fractional difference in r_{50} and concentration as a function of r_{3000} (see Figure 6) for all measurements at $\lambda_r < 1800$ Å. In addition to ensuring that the changes in morphology in the UVIS images are not due to the point spread function, this also helps us isolate the galaxies that are dominating the average trends shown in Figures 4 and 5. While the decrease of r_{50} in the FUV is approximately constant as a function of r_{3000} , concentration only decreases for galaxies with

**Figure 8.** Difference in the 20% light radius (top panel) and the 80% light radius (bottom panel) as a function of r_{3000} for a sample of $0.5 < z < 1.5$ galaxies with $M_{1500} < -17$. Data points are generated in the same way as in Figure 6 and a typical error bar for the individual measurements is given in the lower right corner. The fractional difference in the 20% light radius rises at large r_{3000} , suggesting that the central profiles of large galaxies are flattening in the far-UV. This is likely due to the presence of bulges or proto-bulges in many of the larger objects at $z \sim 1$.

(A color version of this figure is available in the online journal.)

$r_{3000} \gtrsim 2$ kpc. At $z \sim 2$, this effect is still present (Figure 7), but only for larger galaxies ($r_{3000} \gtrsim 4$ kpc).

To better understand the origin of the changes in concentration, we used the Kartaltepe et al. (2014) catalog to obtain H -band visual classifications for 111 galaxies in the $0.5 < z < 1.5$ sample with $H < 24.5$, all with at least four reliable classifications. We define disk galaxies to be those with spheroidicity > 0.5 , where classifiers identified the galaxy as being disk-dominated. By contrast, spheroidal galaxies are those that were considered to be bulge-dominated in the rest-frame optical, or spheroidicity < 0.5 . For spheroidal galaxies, the median change in concentration at $\lambda < 1800$ Å is consistent with zero, ($C - C_{3000} = -0.02 \pm 0.03$), while disk galaxies exhibit a significant drop in concentration over the same wavelength range, with $C - C_{3000} = -0.20 \pm 0.05$. This result suggests that

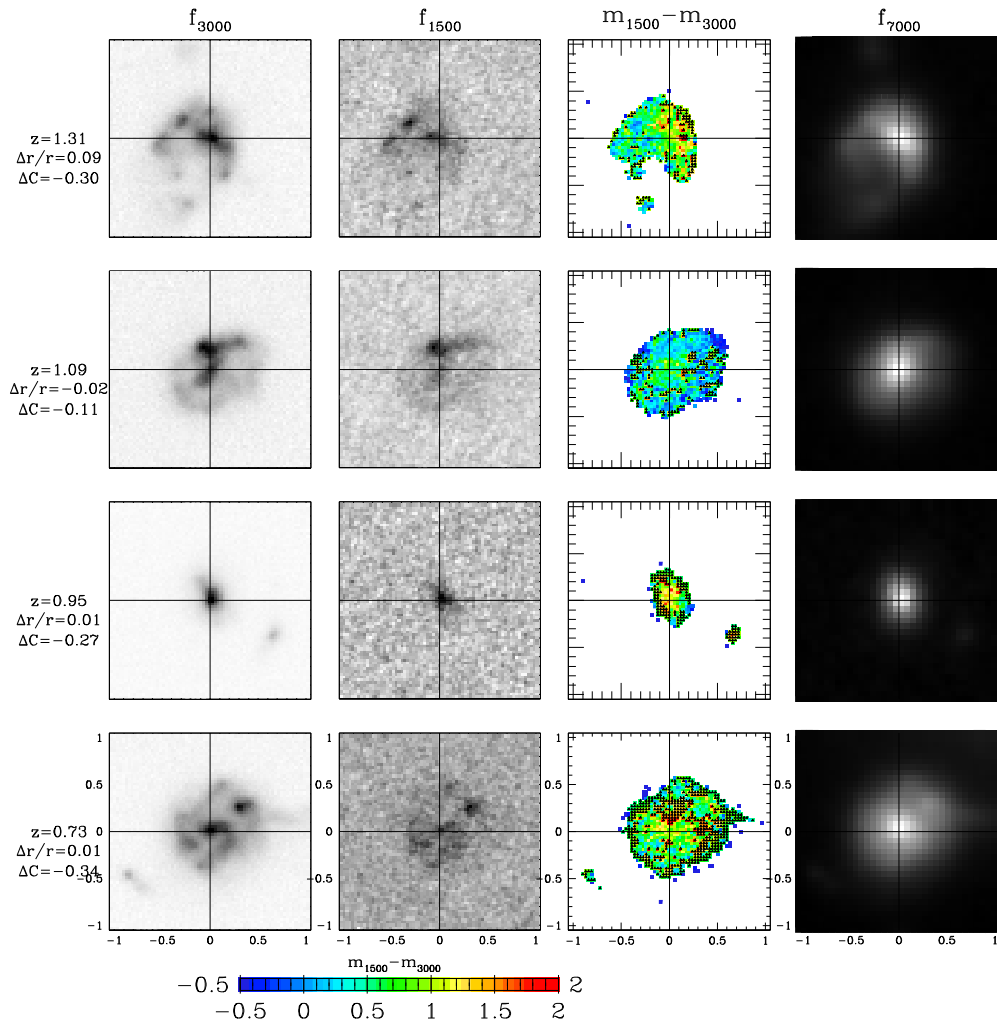


Figure 9. Panels demonstrating the change in morphology of $0.5 < z < 1.5$ galaxies between rest-frame 1500 Å and 3000 Å. We show $2''$ postage stamps of rest-frame 3000 Å (nearest UDF optical image), rest-frame 1500 Å (nearest UVIS image), $m_{1500} - m_{3000}$, and rest-frame 7000 Å (nearest HUDF12 image). The grayscale images are all scaled relative to the minimum and maximum in each panel and the colorscale is given at the bottom. When a pixel is not detected in the UVIS cutout, we color it with the 1σ lower limit and overplot a small black triangle. To the left of each row, we give the galaxy redshift, difference in r_{50} between 1500 Å and 3000 Å, and difference in concentration between 1500 Å and 3000 Å.

(A color version of this figure is available in the online journal.)

the decrease in concentration is occurring primarily in disk-like galaxies.

We can isolate the cause of this change even further by separately analyzing the wavelength dependence of $r_{20\%}$ and $r_{80\%}$ for the galaxies in our sample. Note that the difference in concentration between two wavelengths can be expressed as ΔC , where

$$\Delta C = C_{\lambda_1} - C_{\lambda_2} = 5 \log \left[\frac{r_{80\%,\lambda_1} r_{20\%,\lambda_2}}{r_{80\%,\lambda_2} r_{20\%,\lambda_1}} \right]. \quad (2)$$

A decrease in concentration in the FUV can occur due to a flattening of the inner part of the light profile, $r_{20\%,1500} > r_{20\%,3000}$, or a truncation of the wings, $r_{80\%,1500} < r_{80\%,3000}$, or some combination of both. In Figure 8, we show the difference of these parameters in the FUV as a function of r_{3000} . There is no evidence for a truncation of the outer light profile in the FUV for large galaxies. However, we do find evidence for an increase in the inner radius, with $\Delta r_{20\%}/r_{20\%,3000} = 0.12 \pm 0.03$ for galaxies with $r_{3000} > 2$ kpc compared to galaxies with $r_{3000} < 2$ kpc. This suggests that the trend in Figure 6 is driven by a flattening of the central portion of the light profile, likely due to a decrease-

ing contribution from the bulge of disk-like galaxies further in the FUV.

4. DISCUSSION

Previous studies of star-forming galaxies at $0.5 < z < 1.5$ in the CANDELS survey (Wuyts et al. 2012) revealed that the youngest stellar populations at $0.5 < z < 1.5$ tended to be concentrated in clumps near the effective radius (approximately equivalent to r_{50}). In a simple 1 Gyr constant star formation model, they found that stars < 10 Myr old will contribute $\sim 60\%$ of the FUV light and stars < 100 Myr old will contribute $> 90\%$. Therefore, we expect that young star-forming clumps, when present, will tend to set the physical scale on which both FUV and NUV emission are observed and r_{50} should be approximately constant across this rest-frame wavelength range.

However, far-UV observations of local Sa–Sb galaxies do reveal differences between the 3000 Å and 1500 Å light profiles; in particular, they find that galaxies of type later than S0 exhibit a drop in concentration as one observes further into the FUV (Taylor-Mager et al. 2007). They attribute this change primarily to the diminished brightness of bulges at shorter wavelengths.

Although the fraction of bulge-dominated galaxies decreases with redshift, we still expect $\sim 60\%$ of our galaxies to be bulge-dominated at $z \sim 1$ (Bruce et al. 2012).

Overall, our results are consistent with these expectations, although we do observe a small decrease in r_{50} ($\sim 5\%$) in the FUV for samples at both $0.5 < z < 1.5$ and $1.5 < z < 2.5$. The cause of this decrease is not clear, but it is independent of galaxy size. We also observe a decrease in concentration in the FUV, consistent with results at low redshift. It is only marginal for the sample as a whole ($\Delta C \simeq 0.05$, Figure 5), but the largest galaxies ($r_{3000} > 2$ kpc) exhibit a drop of $\Delta C \simeq -0.3$, which we find to be due to a flattening of the central portion of the light profile for $\lambda < 1800$ Å. A few illustrative examples are shown in Figure 9, where we plot the pixel-by-pixel color maps of four $0.5 < z < 1.5$ galaxies between rest-frame 1500 Å and 3000 Å. We also show NIR cutouts from HUDF12 for comparison. While the majority of the UV emission is blue, with $m_{1500} - m_{3000} \sim 0-1$, the region near the rest-optical centroid tend to be redder than the rest of the galaxy. This is likely due to the presence of a bulge or proto-bulge near the center of the galaxy with older stellar populations and/or more dust than the rest of the galaxy.

To summarize, we find that a 1500 Å luminosity-limited sample of galaxies at $0.5 < z < 1.5$ is both smaller ($\sim 5\%$) and less concentrated ($\Delta C \simeq 0.05$) at 1500 Å compared to 3000 Å. While the wavelength dependence of r_{50} is independent r_{3000} at all redshifts studied, the decrease in concentration is more substantial for galaxies with $r \gtrsim 2$ kpc at $z \sim 1$. At $z \sim 2$, concentration is approximately constant across the rest-UV for all but the largest galaxies ($r \gtrsim 4$ kpc). While we have painted a broad picture of the structural properties of star-forming galaxies in the FUV, a careful analysis of the spatial, size, and color distribution of star-forming clumps is underway (D. F. de Mello et al., in preparation) and should provide us with a more detailed picture of the star formation in these galaxies.

Support for program number HST-GO-12534 was provided by NASA through a grant from the Space Telescope Science Institute, which is operated by the Association of Universities for Research in Astronomy, Inc., under NASA contract NAS 5-26555.

REFERENCES

- Balestra, I., Mainieri, V., Popesso, P., et al. 2010, *A&A*, 512, A12
 Beckwith, S. V. W., Stiavelli, M., Koekemoer, A. M., et al. 2006, *AJ*, 132, 1729

- Benítez, N. 2000, *ApJ*, 536, 571
 Benítez, N., Ford, H., Bouwens, R., et al. 2004, *ApJS*, 150, 1
 Bertin, E., & Arnouts, S. 1996, *A&AS*, 117, 393
 Bournaud, F., & Elmegreen, B. G. 2009, *ApJL*, 694, L158
 Bournaud, F., Elmegreen, B. G., & Elmegreen, D. M. 2007, *ApJ*, 670, 237
 Bruce, V. A., Dunlop, J. S., Cirasuolo, M., et al. 2012, *MNRAS*, 427, 1666
 Coe, D., Benítez, N., Sánchez, S. F., et al. 2006, *AJ*, 132, 926
 Conselice, C. J. 2003, *ApJS*, 147, 1
 Ellis, R. S., McLure, R. J., Dunlop, J. S., et al. 2013, *ApJL*, 763, L7
 Elmegreen, B. G., & Elmegreen, D. M. 2005, *ApJ*, 627, 632
 Ferguson, H. C., Dickinson, M., Giavalisco, M., et al. 2004, *ApJL*, 600, L107
 Ford, H. C., Clampin, M., Hartig, G. F., et al. 2003, *Proc. SPIE*, 4854, 81
 Fruchter, A. S., & Sosey, M. 2009, *The MultiDrizzle Handbook*, version 3.0 (Baltimore, MD: STScI)
 Genzel, R., Burkert, A., Bouché, N., et al. 2008, *ApJ*, 687, 59
 Grogan, N. A., Kocevski, D. D., Faber, S. M., et al. 2011, *ApJS*, 197, 35
 Heckman, T. M., Hoopes, C. G., Seibert, M., et al. 2005, *ApJL*, 619, L35
 Kartaltepe, J. S., et al. 2014, arXiv:1401.2455
 Kent, S. M. 1985, *ApJS*, 59, 115
 Koekemoer, A. M., Fruchter, A. S., Hook, R. N., & Hack, W. 2002, in *The 2002 HST Calibration Workshop: Hubble after the Installation of the ACS and the NICMOS Cooling System*, ed. S. Arribas, A. Koekemoer, & B. Whitmore (Baltimore, MD: STScI), 337
 Koekemoer, A. M., Faber, S. M., Ferguson, H. C., et al. 2011, *ApJS*, 197, 36
 Kuchinski, L. E., Freedman, W. L., Madore, Barry F., et al. 2000, *ApJS*, 131, 441
 Kurk, J., Cimatti, A., Daddi, E., et al. 2013, *A&A*, 549, A63
 Law, D. R., Steidel, C. C., Erb, D. K., et al. 2009, *ApJ*, 697, 2057
 Le Fèvre, O., Vattolani, G., Paltani, S., et al. 2004, *A&A*, 428, 1043
 Lotz, J. M., Madau, P., Giavalisco, M., Primack, J., & Ferguson, H. C. 2006, *ApJ*, 636, 592
 Martin, D. C., Fanson, J., Schiminovich, D., et al. 2005, *ApJL*, 619, L1
 Petrosian, V. 1976, *ApJL*, 209, L1
 Petty, S. M., de Mello, D. F., Gallagher, J. S., et al. 2009, *AJ*, 138, 362
 Popesso, P., Dickinson, M., Nonino, M., et al. 2009, *A&A*, 494, 443
 Rafelski, M., Wolfe, A. M., Cooke, J., et al. 2009, *ApJ*, 703, 2033
 Ravindranath, S., Giavalisco, M., Ferguson, H. C., et al. 2006, *ApJ*, 652, 963
 Rhodes, J., Leauthaud, A., Stoughton, C., et al. 2010, *PASP*, 122, 439
 Robertson, B. E., & Bullock, J. S. 2008, *ApJL*, 685, L27
 Rutkowski, M. J., Cohen, S. H., Kaviraj, S., et al. 2012, *ApJS*, 199, 4
 Shapiro, K. L., Genzel, R., Bouché, N., et al. 2009, in *ASP Conf. Ser. 419, Galaxy Evolution: Emerging Insights and Future Challenges*, ed. S. Jogee, I. Marinova, L. Hao, & G. A. Blanc (San Francisco, CA: ASP), 60
 Spergel, D. N., Bean, R., Doré, O., et al. 2007, *ApJS*, 170, 377
 Szokoly, G. P., Bergeron, J., Hasinger, G., et al. 2004, *ApJS*, 155, 271
 Taylor-Mager, V. A., Conselice, C. J., Windhorst, R. A., & Jansen, R. A. 2007, *ApJ*, 659, 162
 Teplitz, H. I., Rafelski, M., Kurczynski, P., et al. 2013, *AJ*, 146, 159
 van Dokkum, P., Brammer, G., Momcheva, I., et al. 2013, arXiv:1305.2140
 Vanzella, E., Cristiani, S., Dickinson, M., et al. 2005, *A&A*, 434, 53
 Vanzella, E., Cristiani, S., Dickinson, M., et al. 2006, *A&A*, 454, 423
 Vanzella, E., Cristiani, S., Dickinson, M., et al. 2008, *A&A*, 478, 83
 Voyer, E. N. 2011, PhD thesis, The Catholic Univ. America
 Wuyts, S., Förster Schreiber, N. M., Genzel, R., et al. 2012, *ApJ*, 753, 114
 Wuyts, S., Förster Schreiber, N. M., Nelson, E. J., et al. 2013, *ApJ*, 779, 135